ADVANCED FUNCTIONAL MATERIALS
www.afm-journal.de

Mesoporous Carbon Nanocube Architecture for High-Performance Lithium–Oxygen Batteries

*Bing Sun, Shuangqiang Chen, Hao Liu, and Guoxiu Wang**

One of the major challenges to develop high-performance lithium–oxygen ($Li–O_2$) battery is to find effective cathode catalysts and design porous architecture for the promotion of both oxygen reduction reactions and oxygen evolution reactions. Herein, the synthesis of mesoporous carbon nanocubes as a new cathode nanoarchitecture for $Li–O_2$ batteries is reported. The oxygen electrodes made of mesoporous carbon nanocubes contain numerously hierarchical mesopores and macropores, which can facilitate oxygen diffusion and electrolyte impregnation throughout the electrode, and provide sufficient spaces to accommodate insoluble discharge products. When they are applied as cathode catalysts, the $Li–O_2$ cells deliver discharge capacities of 26 100 mA h g^{-1} at 200 mA g^{-1}, which is much higher than that of commercial carbon black catalysts. Furthermore, the mesoporous nanocube architecture can also serve as a conductive host structure for other highly efficient catalysts. For instance, the Ru functionalized mesoporous carbon nanocubes show excellent catalytic activities toward oxygen evolution reactions. $Li–O_2$ batteries with Ru functionalized mesoporous carbon nanocube catalysts demonstrate a high charge/discharge electrical energy efficiency of 86.2% at 200 mA g^{-1} under voltage limitation and a good cycling performance up to 120 cycles at 400 mA g^{-1} with the curtaining capacity of 1000 mA h g^{-1}.

1. Introduction

Recently, rechargeable lithium–oxygen ($Li–O_2$) batteries have attracted intensive investigations due to the highest energy density among all rechargeable battery systems.[1–4] They are considered as one of the most promising power sources to meet the stringent requirements for electric vehicles. However, key limitations, such as large charge/discharge overpotential, low rate capability, and poor cycle life, must be resolved for practical applications.[5,6] In an aprotic rechargeable lithium oxygen battery, oxygen is drawn from the outside atmosphere and reduced by lithium ions from the electrolyte to form discharge products (e.g., Li_2O_2) during the discharge process, which is denoted as oxygen reduction reactions (ORRs). The dominant discharge products electrochemically decompose to lithium ions and oxygen during the charge process, which is denoted as oxygen evolution reactions (OERs).[7,8] The oxygen electrode should consist of porous conductive substrates to accommodate insoluble discharge products and facilitate oxygen diffusion and electrolyte impregnation. The overall energy density is determined by the amount of insoluble discharge products stored in the oxygen electrode.[3] Therefore, it is essential to optimize the porosity of the oxygen electrode to provide large space for insoluble discharge products and facilitate oxygen diffusion and electrolyte impregnation throughout the electrode. Tremendous efforts have been devoted to explore various nanostructured porous catalysts to optimize the porous structure of the oxygen electrode, which also have capability to simultaneously catalyze the ORRs and OERs.[9–11]

Carbon materials have significant advantages to be used as electrode materials for energy storage devices, including light weight, low cost, and abundant resources.[12,13] Nanostructured carbon materials, such as carbon nanotubes, graphene, 3D meso- or macroporous carbon, have been widely used in lithium ion batteries, supercapacitors, and fuel cells.[14–18] They are also the most desired cathode materials for $Li–O_2$ batteries if the side reactions among carbon materials, the discharge products, and electrolyte can be suppressed.[19] Xiao et al. first compared the electrochemical performance of $Li–O_2$ batteries with several different commercial carbon powders.[20] The results indicated that the uniformity of the pore size plays an important role in determining electrochemical performances of $Li–O_2$ batteries. Mitchell et al. reported the use of all carbon nanofiber electrodes for $Li–O_2$ batteries and achieved high gravimetric energies (up to 2500 W h $kg_{discharged}^{-1}$), which is about four times higher than Li-ion batteries with $LiCoO_2$ as cathode materials (≈600 W h $kg_{electrode}^{-1}$).[21] Graphene with different porous architectures was also investigated as cathode materials for $Li–O_2$ batteries by several groups and achieved significantly improved specific discharge capacity.[22–24] 3D-ordered mesoporous/macroporous carbon sphere arrays (MMCSAs) were synthesized and applied as the cathode catalysts in $Li–O_2$ batteries by Guo et al.[25] The ordered mesoporous channels and hierarchical

Dr. B. Sun, Dr. S. Chen, Dr. H. Liu, Prof. G. Wang
Centre for Clean Energy Technology
University of Technology Sydney
Broadway, Sydney NSW 2007, Australia
E-mail: guoxiu.wang@uts.edu.au
Prof. G. Wang
College of Materials Science and Technology
Nanjing University of Aeronautics and Astronautics
Nanjing 210016, P. R. China

DOI: 10.1002/adfm.201500863

mesoporous/macroporous structure of the MMCSAs provide effective spaces for discharge products, which enhanced the electrochemical performance of Li–O_2 batteries. Therefore, the development of porous nanostructures is a promising strategy to improve the electrochemical performance of Li–O_2 batteries.

Another major challenge for the development of high-performance Li–O_2 batteries is to reduce the large charge/discharge overpotential in order to increase the round-trip energy efficiency.[3,26] Although the widely used porous carbon materials can act as good catalysts for ORRs, they are not effective to catalyze the OERs.[22,24,27] Therefore, it is necessary to further functionalize porous carbon materials to increase their catalytic activity toward OERs. A series of carbon-based nanocomposites have been developed to address this challenge, including metal nitrides, metal oxides, or precious metal functionalized carbon materials and doped carbon.[11,28–46]

In this study, we report the synthesis of mesoporous carbon nanocubes (MCCs) as a new cathode nanoarchitecture for Li–O_2 batteries. The oxygen electrodes made of MCCs contain numerously hierarchical mesopores and macropores, which can facilitate oxygen diffusion and electrolyte impregnation throughout the electrode, and provide sufficient spaces to accommodate insoluble discharge products. Li–O_2 batteries with MCC catalysts showed high discharge capacities and excellent high current rate capability. Furthermore, after loading Ru nanocrystals on MCC matrix, the energy efficiency and the cycling stability of Li–O_2 batteries have been significantly improved.

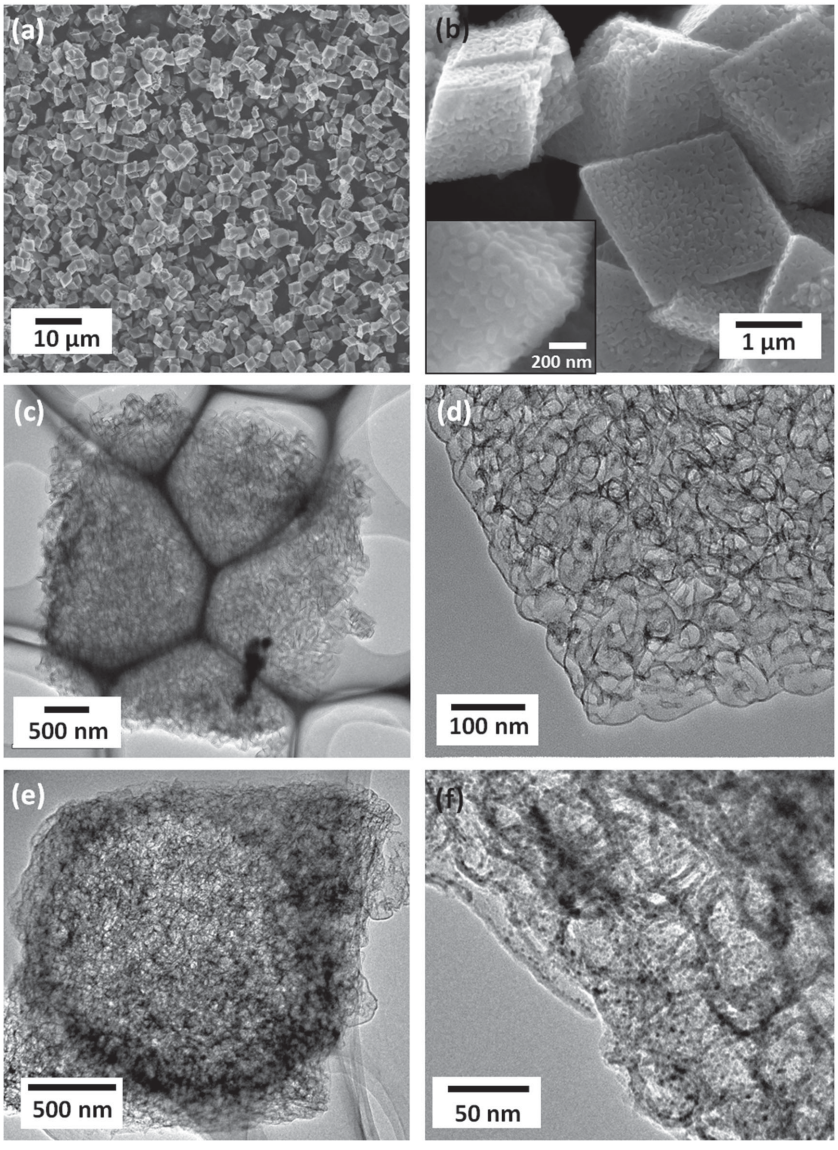

Figure 1. a,b) SEM images of MCCs at different magnifications. c) Low-magnification and d) high-magnification TEM images of MCCs. e) Low-magnification and f) high-magnification TEM images of Ru@MCCs. The inset in (b) shows the porous structure of carbon nanocube at high-magnification.

2. Results and Discussion

MCCs were synthesized by a hard template method. $MnCO_3$ nanocubes were first synthesized by a facile precipitation method. The typical SEM image of $MnCO_3$ is shown in Figure S1a (Supporting Information), which exhibits regular cube structure and smooth surface. After heat treatment, $MnCO_3$ cubes transformed to porous MnO templates (Supporting Information, Figure S1b). The final products of MCCs were obtained via a chemical vapor deposition (CVD) process and the removal of MnO templates by acid etching. The porous architecture of MCCs was first observed by field-emission scanning electron microscopy (FE-SEM) as shown in **Figure 1**. Figure 1a clearly illustrates nanocube architectures. Figure 1b shows the porous structure with many mesopores appeared on the surface of carbon nanocubes. Some of the carbon nanocubes were interconnected with each other. To further confirm the porous architecture of MCCs, transmission electron microscopy (TEM) images at different magnifications are presented in Figure 1c,d. It is observed that MCCs contain many mesopores, which interconnect with each other. The N_2 adsorption–desorption plots of MCCs (**Figure 2**a) show a type IV isotherm with a steep increase of nitrogen absorption at a high relative pressure (P/P_0 = 0.80–0.99), indicating that the main pore volume is contributed by large size pores. The unique architecture of MCCs exhibited a high specific surface area of 492.3 $m^2\ g^{-1}$ and a large pore volume of 3.74 $cm^3\ g^{-1}$. The pore sizes are mainly distributed at about 50 and 100 nm (the inset in Figure 2a).

Ru@MCCs were synthesized by a facile wet impregnation method. MCCs were mixed with an ethanolic solution of $RuCl_3$ by gentle stirring overnight. After dried at room

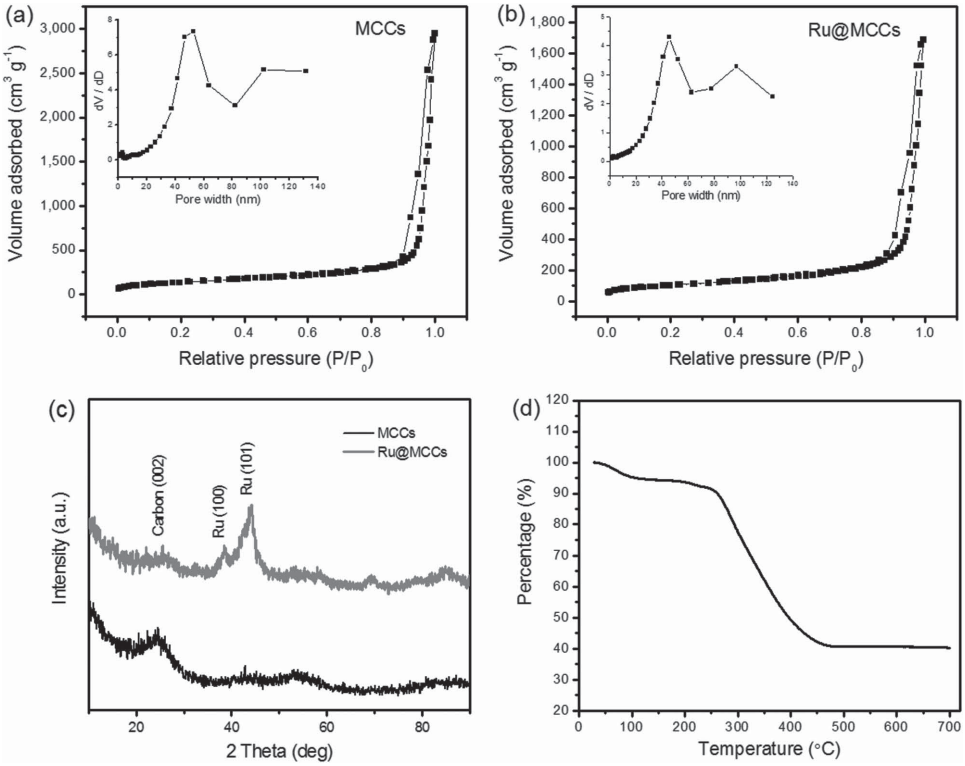

Figure 2. The nitrogen adsorption/desorption isotherms and pore-size distribution of a) MCCs and b) Ru@MCCs. c) XRD patterns of MCCs and Ru@MCCs. d) TGA curve of Ru@MCCs.

temperature under continuous stirring, the obtained precursor was sintered at low temperature in a reduced atmosphere to obtain final products. The TEM image of Ru@MCCs in Figure 1e shows the similar porous structure as that of the pristine MCCs, indicating that the pore structure has been preserved after Ru loading. High-resolution TEM image in Figure 1f clearly shows that Ru nanocrystals are homogeneously distributed on the porous carbon matrix. Figure 2c shows the X-ray diffraction (XRD) patterns of MCCs and Ru@MCCs, in which three diffraction peaks can be indexed to carbon (002), Ru (100), and Ru (101) in the XRD pattern of Ru@MCCs. The Ru content in the Ru@MCC nanocomposite was determined by thermogravimetric analysis (TGA) measurement. The total weight loss of the composite is 60.1 wt% at 600 °C. Counting the oxidation of Ru to RuO_2 at high temperature, the Ru content in the composite is 30.3 wt% (Figure 2d). The N_2 adsorption–desorption plots of Ru@MCCs (Figure 2b) also show a type IV isotherm. The specific surface area of Ru@MCCs is 358.3 m^2 g^{-1} with a pore volume of 2.61 cm^3 g^{-1}. Furthermore, Ru@MCCs shows similar pore-size distribution to MCCs, which confirms that the pore channels of MCCs are not blocked by the loading of Ru nanocrystals.

The electrochemical performance of MCCs as cathode catalysts was examined in aprotic Li–O_2 cells and compared with carbon black (CB) catalysts in the dimethyl sulfoxide (DMSO)-based electrolyte (0.1 M $LiClO_4$ in DMSO). All electrochemical measurement results are normalized based on the total weight of the cathode catalysts. The discharge/charge performances of MCCs and CB catalysts were first examined at 200 mA g^{-1} in the voltage range of 2.0–4.6 V at room temperature (as shown in **Figure 3**a). The MCC electrode achieved a discharge capacity of 26 100 mA h g^{-1}, which is much higher than that of CB electrode (6240 mA h g^{-1}). For the charge process, the charge capacity of the MCC electrode is 16 090 mA h g^{-1}, which is also much higher than that of CB electrode (3933 mA h g^{-1}). Both CB electrode and MCC electrode show capacity decrease in the following cycles (Figure S3, Supporting Information). The capacity fading of Li–O_2 batteries with pristine carbon materials should be caused by the accumulation of by-products in the porous oxygen electrode. Those by-products formed during charge/discharge processes cannot be totally decomposed in the subsequent charge process, which occupy the pore space of the oxygen electrode and induce capacity fading. After the discharge current density increased, the MCC electrode delivered high discharge capacities of 22 390 mA h g^{-1} at 500 mA g^{-1}, 18 280 mA h g^{-1} at 1000 mA g^{-1}, and 12 100 mA h g^{-1} at 2000 mA g^{-1} (Figure 2b). Meanwhile, the CB electrodes exhibited discharge capacities of 4770 mA h g^{-1} at 500 mA g^{-1}, 3530 mA h g^{-1} at 1000 mA g^{-1}, and 2410 mA h g^{-1} at 2000 mA g^{-1} (Figure 2c). The MCC catalysts show capacity retention of 46.3% when the discharge current densities increase from 200 to 2000 mA g^{-1}, which is higher than that of CB catalysts (38.6%) as well as the previously reported porous graphene catalysts (27.8% capacity retention, pore size about 60 nm).[46] The significantly improved high current rate performance of MCC catalysts could be ascribed to the unique hierarchical porous structure of the cathodes, which can facilitate oxygen diffusion, electrolyte impregnation, and accommodation of discharge products during the charge and discharge processes.

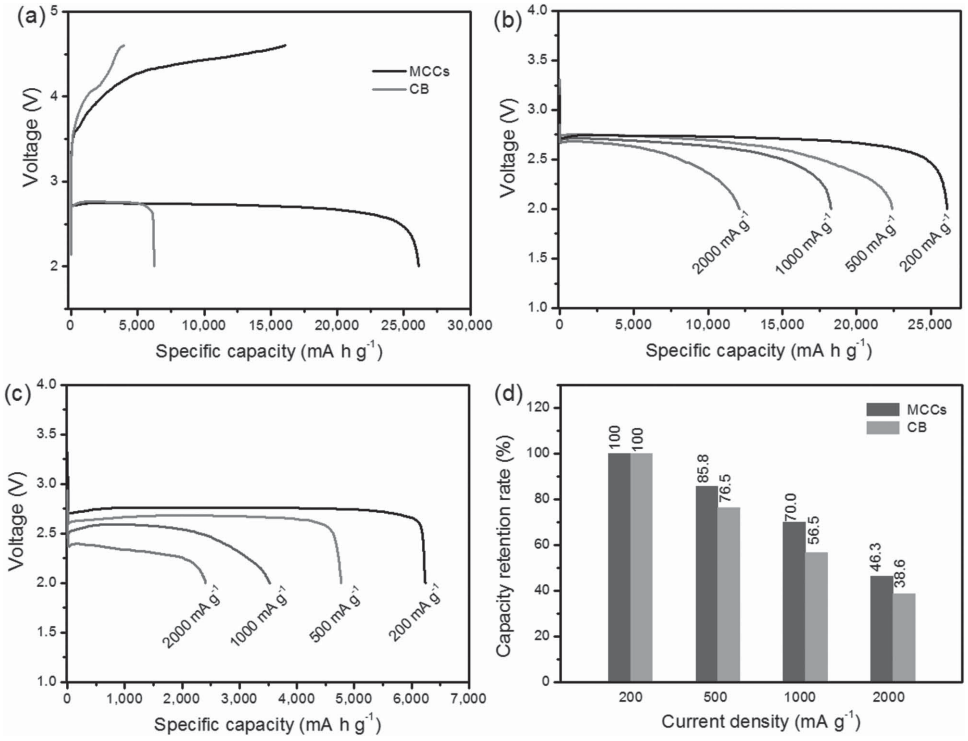

Figure 3. a) The charge/discharge profiles of Li–O_2 cells with MCC and CB catalysts in the first cycle at 200 mA g^{-1} in the voltage range of 2.0–4.6 V in a $LiClO_4$/DMSO electrolyte. Discharge curves of Li–O_2 cells with b) MCC and c) CB catalysts at different current densities in a $LiClO_4$/DMSO electrolyte. d) Capacity retention capability of Li–O_2 cells at different current densities.

The morphologies of the pristine and discharged CB and MCC electrodes were analyzed by FESEM. The SEM observations were performed for electrode at the fully discharge state to 2.0 V and charge state to 4.6 V at the current density of 1000 mA g^{-1}. For the CB electrode, the discharge capacity is 3610 mA h g^{-1} after discharge to 2.0 V at the current density of 1000 mA g^{-1}. For the MCC electrode, the discharge capacity is 18 190 mA h g^{-1} after discharge to 2.0 V at the current density of 1000 mA g^{-1}. From the low-magnification SEM image in **Figure 4**a, we can observe that CB electrode consists of densely agglomerated CB nanoparticles. All nanosized voids of CB electrode are formed between CB nanoparticles (inset in Figure 4a). After discharge to 2.0 V at the current density of 1000 mA g^{-1}, the CB electrode is covered by discharge products with a plate-like shape (Figure 4b,c). While for the MCC electrode discharged to 2.0 V at the current density of 1000 mA g^{-1}, the surface is much rough with many big voids formed between MCCs (Figure 4d). After discharge at the same current density, we observed that carbon nanocubes were covered by toroidal-shape products (Figure 4e,f). Each toroidal discharge product consists of bundles of nanosheets, which is consistent with the previous reports.[21,47] The discharge products of both CB and MCC electrodes after first discharge were analyzed by XRD as shown in Figure S2 (Supporting Information). The dominant discharge products after the first discharge can be identified to be Li_2O_2 for both electrodes. This indicates that the dominant reactions in DMSO-based electrolyte are ORRs. Based on the ex situ SEM analysis, we can conclude that the structure of oxygen electrodes can significantly influence the morphology of Li_2O_2 formation during the ORRs.

The previous report demonstrated that the growth mechanism of Li_2O_2 in Li–O_2 batteries depends on the current rate that governs the electrochemical pathway.[48] Low current density favors the formation of large toroidal nanocrystalline peroxide aggregates via solution dismutase on the surface of the electrode. With the increase of the current density, the number of toroids increases and their relative size decreases. At high current densities, Li_2O_2 favors to form thin film with much less crystalline product. The significant differences of the morphology of Li_2O_2 on different electrodes imply that the actual current density during the Li_2O_2 formation should be different with the increase of the depth of discharge. The schematic illustrations of the electrode morphology changes before and after discharge are shown in **Figure 5**. For the CB electrode, the nanopores are formed between CB nanoparticles. During the discharge process, the nanopores are easily to be blocked by the discharge products in the initial discharge process. Only the surface of the CB electrode maintains active for further Li_2O_2 formation (Figure 5a). This means that the actual local current density for the Li_2O_2 growth becomes significantly higher than that at the initial discharge stage after the nanopores inside the electrode are blocked. After fully discharging the CB electrode to 2.0 V, we observed that the plate-shape Li_2O_2 grew on the surface of the electrode, which is much smaller than that grew on the MCC electrode (Figure 4c,f). The MCC electrode consists of carbon nanocubes (Figure 5b). Each carbon nanocube contains numerous mesopores, which can facilitate the electrolyte

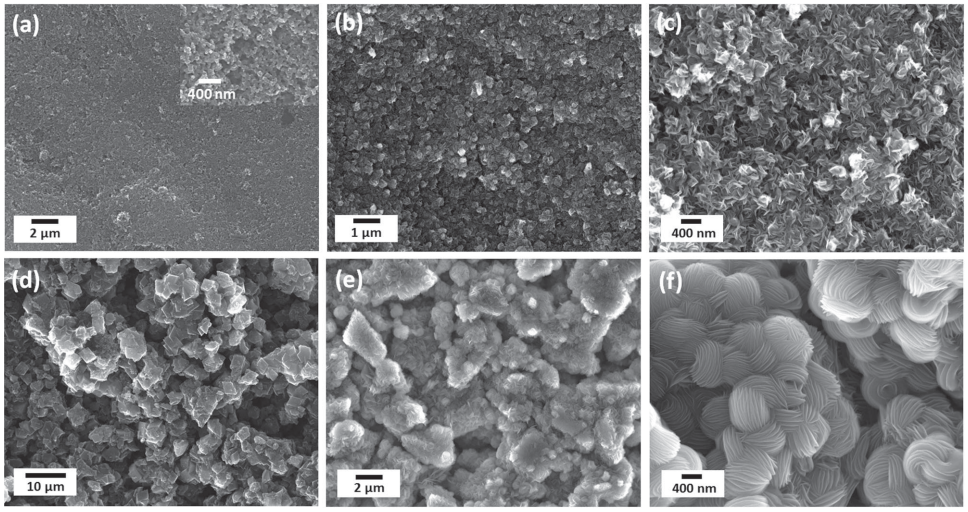

Figure 4. SEM images of a) pristine and b,c) first discharged CB electrodes, d) pristine and e,f) first discharged MCC electrodes in the $LiClO_4$/DMSO electrolyte. The inset in (a) is high-magnification SEM image of pristine CB electrode.

impregnation and oxygen diffusion. Furthermore, large amount of macropores is also formed between carbon nanocubes. After discharging the MCC electrode at relatively high current density (1000 mA g^{-1}), large amount of discharge products was randomly deposited on the porous oxygen electrode (Figure 5b). The mesopores inside carbon nanocubes can be easily chocked during the discharge process. However, the macropores are difficult to be blocked even after fully discharging the electrode to 2.0 V (Figure 4f). There are enough spaces inside the oxygen electrode for the growth of toroidal-shaped Li_2O_2 on the surface of carbon nanocubes (Figure 5b). Therefore, the MCC electrode containing macropores and mesopores showed higher discharge capacity and better rate capability than the CB electrode with only nanopores. The galvanostatic charge/discharge test and SEM analysis of the pristine and discharged electrodes clearly illustrated that the pore-size structure of the oxygen electrode is essential to improve the electrochemical performance of Li–O_2 batteries.

As reported previously, the OER activity of carbon materials is not sufficient for high-performance Li–O_2 batteries.[9,17,22,30] It is a promising strategy through functionalization of porous carbon materials with other high OER catalysts to form porous nanocomposites. Ru nanocrystals have been demonstrated to be an effective cathode catalyst for OERs in aprotic electrolyte.[40–42,44–46] Therefore, we further loaded Ru nanocrystals on MCCs to enhance the OER activity. The galvanostatic charge/discharge measurements were carried out to evaluate the electrochemical performances of Ru@MCCs at room temperature. The electrolyte, 1.5 M $LiNO_3$ in DMSO ($LiNO_3$/DMSO), was used, which has a good stability toward lithium metal anode and forms a stable solid-electrolyte interphase layer between the lithium anode and electrolyte.[49] Li–O_2 cells with pristine MCC catalysts were also tested in the same condition as a comparison. **Figure 6**a shows the charge/discharge voltage profiles of different catalysts in the first cycle under voltage limitation. As shown in Figure S4 (Supporting Information), the discharge

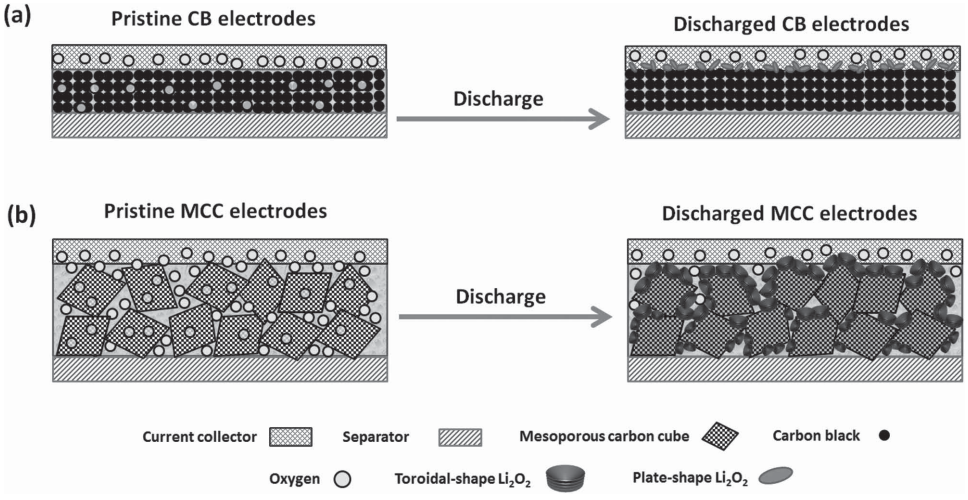

Figure 5. Schematic illustrations of the electrode morphology changes before and after discharge. a) The deposition process of plate-shape Li_2O_2 on the CB electrodes. b) The deposition process of toroidal-shape Li_2O_2 on the MCC electrodes.

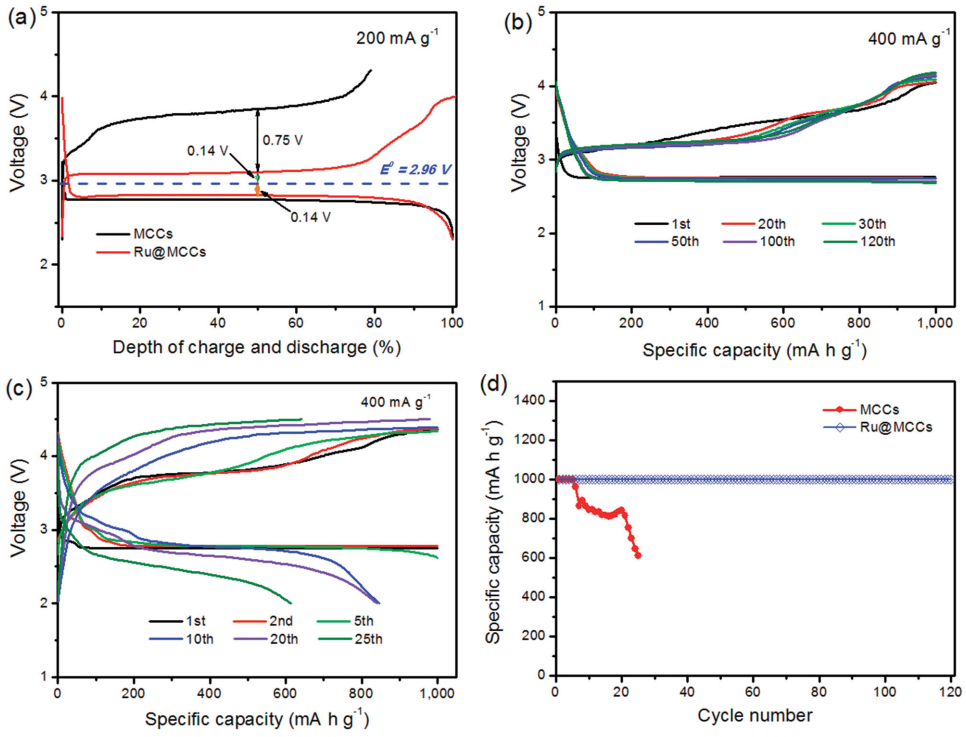

Figure 6. a) Charge/discharge profiles of Li–O_2 batteries with Ru@MCC and MCC as cathode catalysts at 200 mA g^{-1} under voltage limitation in a $LiNO_3$/DMSO electrolyte. Charge/discharge profiles at different cycles of Li–O_2 battery with b) Ru@MCC and c) MCC catalysts at 400 mA g^{-1} by curtailing the capacity to 1000 mA h g^{-1} in the voltage range of 2.0–4.5 V in a $LiNO_3$/DMSO electrolyte. d) The discharge and charge capacity versus cycle number in (b) and (c).

capacity and voltage plateau of the MCC electrode in $LiNO_3$/DMSO electrolyte are similar to that in $LiClO_4$/DMSO electrolyte (Figure 3a). However, during the subsequent charge process, the MCC electrode shows much lower charge overpotential in $LiNO_3$/DMSO electrolyte than that in $LiClO_4$/DMSO electrolyte (Figures 3a and 6a). The significantly decreased charge voltage plateau in $LiNO_3$/DMSO electrolyte compared with that in $LiClO_4$/DMSO electrolyte could be ascribed to the NO_2^-/NO_3^- redox couple, which acts as a soluble electrocatalyst during the charge process.[49] For the Ru@MCC electrode, the discharge plateau of Ru@MCC electrode is 2.82 V at 200 mA g^{-1}, which is higher than that of MCC electrode (2.68 V). Furthermore, the Ru@MCC electrode shows a charge voltage plateau at 3.1 V with the charge overpotential of 0.14 V. The energy efficiency of Ru@MCC electrode in the first cycle is 86.2%, which is also much higher than that of MCC electrodes. Recent report from Bruce's group clarified that the side reactions between carbon materials and the discharge products and electrolytes significantly increased after the charge voltage increased above 3.5 V in DMSO-based electrolyte.[50] The Ru@MCC catalysts can significantly decrease most of the charge potential under 3.5 V, which is crucial to stabilize the operation of Li–O_2 batteries.[8,41,44,46]

The ORR mechanism in the discharge process has been intensively studied. In the presence of lithium ions in a non-aqueous electrolyte, the reduction of oxygen first forms LiO_2 as the intermediate. Then, the unstable LiO_2 disproportionates to Li_2O_2 or reacts with another Li^+ to form Li_2O_2.[7,48] In the charge process, the decomposition of Li_2O_2 during the charge process could undergo through two different pathways.[51,52] The first pathway is associated with the delithiation of Li_2O_2 to form LiO_2-like species in the first step via a solid-solution route (Equation (1)). In the second step, the metastable LiO_2 disproportionates to evolve O_2, yielding an overall $2e^-/O_2$ oxygen evolution process (Equation (2)). The second pathway involves direct electrochemical decomposition of Li_2O_2 to form Li^+ and O_2 via a two-phase transition (Equation (3))

$$Li_2O_2 \rightarrow Li^+ + e^- + LiO_2 \quad (1)$$

$$LiO_2 + LiO_2 \rightarrow Li_2O_2 + O_2 \quad (2)$$

$$Li_2O_2 \rightarrow 2Li^+ + 2e^- + O_2 \quad (3)$$

The charge overpotential of the decomposition of Li_2O_2 through the first pathway is much lower than that through the second pathway. The low charge overpotential of Ru@MCC electrode (0.14 V) implies that the deposition of Li_2O_2 should follow the delithiation mechanism.

The cycling performances of Ru@MCC catalysts were first examined in the voltage range of 2.0–4.1 V at 1000 mA g^{-1} (Figure S5, Supporting Information). Even at an increased charge/discharge current density, the Ru@PGE-2 catalysts still achieved a charge voltage plateau lower than 4.0 V. The cycling performances of Li–O_2 batteries with Ru@MCC and MCC catalysts were further investigated under capacity limitation. Figure 6b shows the charge/discharge profiles of the Ru@MCC electrode at 400 mA g^{-1} by curtailing the capacity to 1000 mA h g^{-1}.

There is no significant change of the charge/discharge voltage profiles and loss of specific capacity up to 120 cycles, indicating the excellent reversibility of the Ru@MCC electrode. The Ru@MCC electrode also show high energy efficiency of 79.82% in the first cycle, which is still maintained at 79.83% at the 120th cycle (Figure S6, Supporting Information). The energy efficiency of the Ru@MCC electrode in $LiNO_3$/DMSO electrolyte is higher than the previous reports.[41–46] For the bare MCC electrode, the discharge voltage plateau began to decrease from the fifth cycle and the discharge capacity dramatically decreased after the sixth cycle (Figure 6c,d).

The morphologies of the discharged and charged Ru@MCC electrodes under capacity limitation were further analyzed by FE-SEM. After discharging the cell to 1000 mA h g^{-1} in the first cycle, many Li_2O_2 nanoplates were anchored on the surface of the porous carbon nanocubes (**Figure 7**a). After first charge, all the discharge products disappeared (Figure 7b). The Fourier transform infrared spectroscopy (FTIR) spectra in Figure S7 (Supporting Information) further demonstrated the formation and decomposition of Li_2O_2 after first discharge and charge. In the 50th cycle, we also observed the formation and decomposition of Li_2O_2 nanoplates by FESEM images (Figure 7c,d). The FTIR spectra in Figure S7 (Supporting Information) also demonstrated the formation and decomposition of Li_2O_2 and other byproducts in the 50th discharge and charge. The SEM observation and FTIR measurement indicate that the dominant reactions of Li–O_2 batteries with Ru@MCC catalysts are the ORRs and OERs during cycling. The above results demonstrate that Li–O_2 cells with Ru@MCC catalysts can operate reversibly with high energy efficiency, and good cycling stability under the curtailing capacity. The significantly improved electrochemical performance could be attributed to the unique architecture of MCCs combined with the highly efficient Ru nanocrystal catalysts. MCCs provide sufficient spaces to accommodate the discharge products, thus effectively reducing the volume change during the charge/discharge. Furthermore, the Ru nanocrystals can significantly reduce the charge overpotential. This effect not only increases the energy efficiency but also reduces the electrolyte decomposition at high charge voltages.[50] Therefore, the Li–O_2 batteries with Ru@MCC catalysts exhibit excellent cycling performance during charge/discharge.

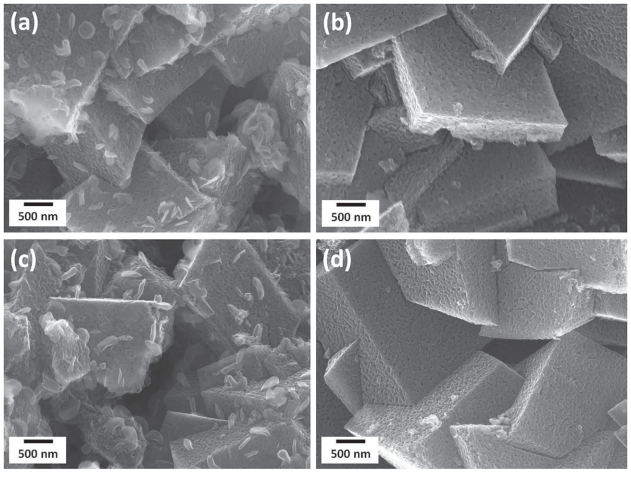

Figure 7. SEM images of Ru@MCC electrodes at different discharge/charge states cycling at 400 mA g^{-1} by curtailing the capacity to 1000 mA h g^{-1} in a $LiNO_3$/DMSO electrolyte. a) After first discharge, b) after first charge, c) after 50th discharge, and d) after 50th charge. The insets in (a) and (c) show the toroidal-shaped discharge product at high magnification.

3. Conclusion

In summary, MCCs were successfully synthesized by a hard template method through a CVD process. MCCs contain not only numerously mesopores but also large amount of macropores formed between individual carbon nanocubes. The hierarchical pore structure in the oxygen electrode could facilitate the oxygen diffusion and electrolyte impregnation and provide large space to accommodate insoluble discharge products (e.g., Li_2O_2). Li–O_2 batteries with MCCs as cathode catalysts delivered a discharge capacity of 26 100 mA h g^{-1} at 200 mA g^{-1} and 12 100 mA h g^{-1} at 2000 mA g^{-1}, demonstrating a good oxygen reduction activity. After functionalized with Ru nanocrystals, the Ru-loaded carbon nanocube composite catalysts exhibit a significantly reduced charge overpotential, high round-trip energy efficiency, and excellent cycling stability.

4. Experimental Section

Materials Preparation: MCCs were synthesized through a hard template method. $MnCO_3$ cubes were synthesized in the first step. In a typical synthesis process: 3.5 mmol $MnSO_4{\cdot}H_2O$, 100 mmol $(NH_4)_2SO_4$, and 35 mL ethanol were dissolved in 350 mL deionized water under strong stirring at 50 °C. Then, 350 mL $(NH_4)_2CO_3$ solution (0.15 M) was added into the above solution under vigorous stirring for 9 h. The precipitation was collected by filtration, washed with deionized water several times and dried at 80 °C under vacuum for 12 h. MnO cubes were obtained after annealing the precursor at 600 °C for 5 h in air. Carbon-coated mesoporous MnO cubes were synthesized via a chemical vapor deposition (CVD) method: MnO nanocubes were placed in a quartz tube furnace and preheated to 650 °C in Ar atmosphere. Then, acetylene (10 vol% in Ar) was introduced with a flow rate of 100 sccm for 1 h. After cooling down to room temperature, the obtained composite was washed with 1 M HCl for 24 h to remove MnO templates. MCCs were obtained after washed by distilled water and dried at 80 °C in a vacuum oven overnight. Ruthenium functionalized MCCs were prepared by an impregnation method. MCCs (35 mg) were dispersed in $RuCl_3$ (Ru, 15.0 mg)/ethanol (10 mL) solution with constant gentle stirring at room temperature for 24 h in a sealed bottle. Then the bottle was opened and the mixture was dried under room temperature with continuous stirring. The dried sample was then heat treated at 300 °C for 3 h under 5% H_2/Ar atmosphere to obtain the final product.

Characterization: Field-emission scanning electron microscopy (FE-SEM, Zeiss Supra 55VP) and transmission electron microscopy (TEM, model JEM-2011, JEOL) were used to investigate the morphologies of the as-prepared materials and the air electrode before and after discharge. XRD pattern measurement was conducted on a Siemens D5000 X-ray diffractometer using Cu Kα radiation. During the XRD analysis, the discharged cathode electrodes were enclosed in a thin transparent polymer film to reduce their exposure to the ambient atmosphere. Nitrogen-sorption measurements were carried out at 77 K with a Micromeritics 3Flex surface characterization analyzer. The Brunauer-Emmett-Teller (BET) method was used to calculate the specific surface area. The pore-size distribution was derived from the adsorption branch of the isotherm by using the Barrett–Joyner–Halenda method. The total pore volume was calculated from the amount adsorbed at a maximum relative pressure, P/P_0. Thermogravimetric analysis

was carried out using a TA Instruments SDT 2960 at a heating rate of 10 °C min^{-1} in air. Infrared spectroscopy was carried out using an Agilet Cary 630 spectrometer in an argon-filled glove box.

Electrochemical Measurements: The oxygen diffusion electrodes were prepared by the following procedure. The catalyst slurry was prepared by mixing the as-prepared catalysts (90 wt%) with poly(tetrafluoroethylene) (10 wt%) in isopropanol. The mixture was then coated on a glass fiber separator. The cathode film was punched into discs with a diameter of 14 mm and dried at 110 °C in a vacuum oven for 12 h. The typical loading of the air electrode is about 0.5 $mg_{catalyst}$ cm^{-2}. Swagelok-type cell with an air hole (0.785 cm^2) on the cathode side was used to investigate the charge/discharge performance. The Li–O_2 cells were assembled in an Ar-filled glove box (Mbraun) with water and oxygen level less than 0.1 ppm. A lithium foil was used as the anode and was separated by a glass microfiber filter, soaked in 0.1 M $LiClO_4$ or 1.5 M $LiNO_3$ in dimethyl sulfoxide electrolyte. Li foils were kept in 0.1 M $LiClO_4$/propylene carbonate electrolyte with 5 vol% fluoroethylene carbonate for 3 d before being used as the anode in Li–O_2 cells containing 0.1 M $LiClO_4$/DMSO electrolytes. The Li foils were rinsed with DMSO to remove any residual carbonate electrolytes. For the Li–O_2 cells containing 1.5 M $LiNO_3$/DMSO electrolytes, the Li foils were directly used without treatment. The anhydrous DMSO solvent was distilled by 4 Å molecular sieves for several weeks and $LiClO_4$ and $LiNO_3$ was dried under vacuum at 150 °C before use. The cell was gas-tight except for the stainless steel mesh window that exposed the porous cathode film to the oxygen atmosphere. All measurements were conducted in 1 atm dry oxygen atmosphere to avoid any negative effects of humidity and CO_2. Galvanostatic discharge/charge was conducted on a Neware battery testing system. The current densities and specific capacities were calculated based on the total mass of catalysts in the electrodes.

Supporting Information

Supporting Information is available from the Wiley Online Library or from the author.

Acknowledgements

This project was financially supported by the Australian Research Council (ARC) through the ARC FT project (FT110100800) and the Fundamental Research Funds for the Central Universities of China (NE2014301).

Received: March 3, 2015
Revised: March 17, 2015
Published online: June 10, 2015

[1] K. M. Abraham, Z. Jiang, *J. Electrochem. Soc.* **1996**, *143*, 1.
[2] P. G. Bruce, S. A. Freunberger, L. J. Hardwick, J. M. Tarascon, *Nat. Mater.* **2012**, *11*, 19.
[3] G. Girishkumar, B. McCloskey, A. C. Luntz, S. Swanson, W. Wilcke, *J. Phys. Chem. Lett.* **2010**, *1*, 2193.
[4] J. Lu, L. Li, J.-B. Park, Y.-K. Sun, F. Wu, K. Amine, *Chem. Rev.* **2014**, *114*, 5611.
[5] J. Christensen, P. Albertus, R. S. Sanchez-Carrera, T. Lohmann, B. Kozinsky, R. Liedtke, J. Ahmed, A. Kojic, *J. Electrochem. Soc.* **2012**, *159*, R1.
[6] F. J. Li, T. Zhang, H. S. Zhou, *Energy Environ. Sci.* **2013**, *6*, 1125.
[7] Z. Q. Peng, S. A. Freunberger, L. J. Hardwick, Y. H. Chen, V. Giordani, F. Barde, P. Novak, D. Graham, J. M. Tarascon, P. G. Bruce, *Angew. Chem. Int. Ed.* **2011**, *50*, 6351.
[8] Z. Q. Peng, S. A. Freunberger, Y. H. Chen, P. G. Bruce, *Science* **2012**, *337*, 563.
[9] J.-J. Xu, Z.-L. Wang, D. Xu, F.-Z. Meng, X.-B. Zhang, *Energy Environ. Sci.* **2014**, *7*, 2213.
[10] J. J. Xu, Z. L. Wang, D. Xu, L. L. Zhang, X. B. Zhang, *Nat. Commun.* **2013**, *4*, 3438.
[11] J. Wang, Y. Li, X. Sun, *Nano Energy* **2013**, *2*, 443.
[12] S. Flandrois, B. Simon, *Carbon* **1999**, *37*, 165.
[13] E. Frackowiak, F. Beguin, *Carbon* **2001**, *39*, 937.
[14] E. Frackowiak, F. Beguin, *Carbon* **2002**, *40*, 1775.
[15] Y. Zhu, S. Murali, M. D. Stoller, K. J. Ganesh, W. Cai, P. J. Ferreira, A. Pirkle, R. M. Wallace, K. A. Cychosz, M. Thommes, D. Su, E. A. Stach, R. S. Ruoff, *Science* **2011**, *332*, 1537.
[16] E. Yoo, J. Kim, E. Hosono, H.-s. Zhou, T. Kudo, I. Honma, *Nano Lett.* **2008**, *8*, 2277.
[17] G. Wang, H. Liu, J. Liu, S. Qiao, G. M. Lu, P. Munroe, H. Ahn, *Adv. Mater.* **2010**, *22*, 4944.
[18] R. Liu, D. Wu, X. Feng, K. Muellen, *Angew. Chem. Int. Ed.* **2010**, *49*, 2565.
[19] S. J. Kang, T. Mori, S. Narizuka, W. Wilcke, H.-C. Kim, *Nat. Commun.* **2014**, *5*.
[20] J. Xiao, D. H. Wang, W. Xu, D. Y. Wang, R. E. Williford, J. Liu, J. G. Zhang, *J. Electrochem. Soc.* **2010**, *157*, A487.
[21] R. R. Mitchell, B. M. Gallant, C. V. Thompson, Y. Shao-Horn, *Energy Environ. Sci.* **2011**, *4*, 2952.
[22] Y. L. Li, J. J. Wang, X. F. Li, D. S. Geng, R. Y. Li, X. L. Sun, *Chem. Commun.* **2011**, *47*, 9438.
[23] J. Xiao, D. H. Mei, X. L. Li, W. Xu, D. Y. Wang, G. L. Graff, W. D. Bennett, Z. M. Nie, L. V. Saraf, I. A. Aksay, J. Liu, J. G. Zhang, *Nano Lett.* **2011**, *11*, 5071.
[24] B. Sun, B. Wang, D. W. Su, L. D. Xiao, H. Ahn, G. X. Wang, *Carbon* **2012**, *50*, 727.
[25] Z. Guo, D. Zhou, X. Dong, Z. Qiu, Y. Wang, Y. Xia, *Adv. Mater.* **2013**, *25*, 5668.
[26] J. Liu, R. Younesi, T. Gustafsson, K. Edström, J. Zhu, *Nano Energy* **2014**, *10*, 19.
[27] H. G. Jung, J. Hassoun, J. B. Park, Y. K. Sun, B. Scrosati, *Nat. Chem.* **2012**, *4*, 579.
[28] Y. Y. Shao, S. Park, J. Xiao, J. G. Zhang, Y. Wang, J. Liu, *ACS Catal.* **2012**, *2*, 844.
[29] F. J. Li, R. Ohnishi, Y. Yamada, J. Kubota, K. Domen, A. Yamada, H. S. Zhou, *Chem. Commun.* **2013**, *49*, 1175.
[30] R. Black, J. H. Lee, B. Adams, C. A. Mims, L. F. Nazar, *Angew. Chem. Int. Ed.* **2013**, *52*, 392.
[31] H. L. Wang, Y. Yang, Y. Y. Liang, G. Y. Zheng, Y. G. Li, Y. Cui, H. J. Dai, *Energy Environ. Sci.* **2012**, *5*, 7931.
[32] B. Sun, H. Liu, P. Munroe, H. Ahn, G. X. Wang, *Nano Res.* **2012**, *5*, 460.
[33] Y. Cao, Z. K. Wei, J. He, J. Zang, Q. Zhang, M. S. Zheng, Q. F. Dong, *Energy Environ. Sci.* **2012**, *5*, 9765.
[34] Y. C. Lu, Z. C. Xu, H. A. Gasteiger, S. Chen, K. Hamad-Schifferli, Y. Shao-Horn, *J. Am. Chem. Soc.* **2010**, *132*, 12170.
[35] J. Lu, Y. Lei, K. C. Lau, X. Y. Luo, P. Du, J. G. Wen, R. S. Assary, U. Das, D. J. Miller, J. W. Elam, H. M. Albishri, D. Abd El-Hady, Y. K. Sun, L. A. Curtiss, K. Amine, *Nat. Commun.* **2013**, *4*, 2383.
[36] D. Oh, J. F. Qi, Y. C. Lu, Y. Zhang, Y. Shao-Horn, A. M. Belcher, *Nat. Commun.* **2013**, *4*, 2756.
[37] Y. L. Li, J. J. Wang, X. F. Li, D. S. Geng, M. N. Banis, R. Y. Li, X. L. Sun, *Electrochem. Commun.* **2012**, *18*, 12.
[38] Y. L. Li, J. J. Wang, X. F. Li, J. Liu, D. S. Geng, J. L. Yang, R. Y. Li, X. L. Sun, *Electrochem. Commun.* **2011**, *13*, 668.
[39] H. Nie, H. Zhang, Y. Zhang, T. Liu, J. Li, Q. Lai, *Nanoscale* **2013**, *5*, 8484.
[40] H. G. Jung, Y. S. Jeong, J. B. Park, Y. K. Sun, B. Scrosati, Y. J. Lee, *ACS Nano* **2013**, *7*, 3532.
[41] B. Sun, P. Munroe, G. X. Wang, *Sci. Rep.* **2013**, *3*, 2247.

[42] F. Li, D.-M. Tang, Y. Chen, D. Golberg, H. Kitaura, T. Zhang, A. Yamada, H. Zhou, *Nano Lett.* **2013**, *13*, 4702.
[43] E. Yilmaz, C. Yogi, K. Yamanaka, T. Ohta, H. R. Byon, *Nano Lett.* **2013**, *13*, 4679.
[44] F. Li, D.-M. Tang, Z. Jian, D. Liu, D. Golberg, A. Yamada, H. Zhou, *Adv. Mater.* **2014**, *26*, 4659.
[45] F. Li, Y. Chen, D.-M. Tang, Z. Jian, C. Liu, D. Golberg, A. Yamada, H. Zhou, *Energy Environ. Sci.* **2014**, *7*, 1648.
[46] B. Sun, X. Huang, S. Chen, P. Munroe, G. Wang, *Nano Lett.* **2014**, *14*, 3145.
[47] M. M. Ottakam Thotiyl, S. A. Freunberger, Z. Peng, Y. Chen, Z. Liu, P. G. Bruce, *Nat. Mater.* **2013**, *12*, 1050.
[48] B. D. Adams, C. Radtke, R. Black, M. L. Trudeau, K. Zaghib, L. F. Nazar, *Energy Environ. Sci.* **2013**, *6*, 1772.
[49] B. Sun, X. Huang, S. Chen, J. Zhang, G. Wang, *RSC Adv.* **2014**, *4*, 11115.
[50] M. M. O. Thotiyl, S. A. Freunberger, Z. Peng, P. G. Bruce, *J. Am. Chem. Soc.* **2013**, *135*, 494.
[51] S. Kang, Y. Mo, S. P. Ong, G. Ceder, *Chem. Mater.* **2013**, *25*, 3328.
[52] Y.-C. Lu, Y. Shao-Horn, *J. Phys. Chem. Lett.* **2013**, *4*, 93.